

BEER analysis of *Kepler* and CoRoT light curves:

I. Discovery of Kepler-76b: A hot Jupiter with evidence for superrotation

S. Faigler¹, L. Tal-Or¹, T. Mazeh¹, D. W. Latham² and L. A. Buchhave³

ABSTRACT

We present the first case in which the BEER algorithm identified a hot Jupiter in the *Kepler* light curve, and its reality was confirmed by orbital solutions based on follow-up spectroscopy. Kepler-76b was identified by the BEER algorithm, which detected the BEaming (sometimes called Doppler boosting) effect together with the Ellipsoidal and Reflection/emission modulations (BEER), at an orbital period of 1.54 days, suggesting a planetary companion orbiting the 13.3 mag F star. Further investigation revealed that this star appeared in the *Kepler* eclipsing binary catalog with estimated primary and secondary eclipse depths of 5×10^{-3} and 1×10^{-4} respectively. Spectroscopic radial-velocity follow-up observations with TRES and SOPHIE confirmed Kepler-76b as a transiting $2.0 \pm 0.26 M_{\text{Jup}}$ hot Jupiter. The mass of a transiting planet can be estimated from either the beaming or the ellipsoidal amplitude. The ellipsoidal-based mass estimate of Kepler-76b is consistent with the spectroscopically measured mass while the beaming-based estimate is significantly inflated. We explain this apparent discrepancy as evidence for the superrotation phenomenon, which involves eastward displacement of the hottest atmospheric spot of a tidally-locked planet by an equatorial super-rotating jet stream. This phenomenon was previously observed only for HD 189733b in the infrared. We show that a phase shift of 10.3 ± 2.0 degrees of the planet reflection/emission modulation, due to superrotation, explains the apparently inflated beaming modulation, resolving the ellipsoidal/beaming amplitude discrepancy. Kepler-76b is one of very few confirmed planets in the *Kepler* light curves that show BEER modulations and the first to show superrotation evidence in the *Kepler* band. Its discovery illustrates for the first time the ability of the BEER algorithm to detect short-period planets and brown dwarfs.

¹ School of Physics and Astronomy, Raymond and Beverly Sackler Faculty of Exact Sciences, Tel Aviv University, Tel Aviv 69978, Israel

² Harvard-Smithsonian Center for Astrophysics, 60 Garden St., Cambridge, MA 02138

³ Niels Bohr Institute, University of Copenhagen, DK-2100 Copenhagen, Denmark

Subject headings: binaries: spectroscopic — methods: data analysis — planets and satellites: detection — stars: individual (Kepler-76, KIC 4570949)

1. Introduction

CoRoT and *Kepler* have produced hundreds of thousands of nearly uninterrupted high precision light curves (Auvergne et al. 2009; Koch et al. 2010) that enable detection of minute astrophysical effects. One of these is the the beaming effect, sometimes called Doppler boosting, induced by stellar radial velocity. The effect causes a decrease (increase) of the brightness of any light source receding from (approaching) the observer (Rybicki & Lightman 1979), on the order of $4v_r/c$, where v_r is the radial velocity of the source, and c is the velocity of light. Thus, periodic variation of the stellar radial velocity due to an orbiting companion produces a periodic beaming modulation of the stellar flux. Loeb & Gaudi (2003) and Zucker, Mazeh & Alexander (2007) suggested to use this effect to identify *non-eclipsing* binaries and exoplanets in the light curves of CoRoT and *Kepler*. The precision of the two satellites is needed because even for short-period binaries, with large radial-velocity (RV) orbital amplitudes, the beaming effect is small, on the order of 100–500 ppm (parts per million).

As predicted, several studies identified the beaming effect in short-period known eclipsing binaries (van Kerkwijk et al. 2010; Rowe et al. 2011; Carter et al. 2011; Kipping & Spiegel 2011; Bloemen et al. 2011, 2012; Breton et al. 2012; Weiss et al. 2012). Yet, space missions data can be used to identify *non-eclipsing* binaries through detection of the beaming effect (Loeb & Gaudi 2003; Zucker, Mazeh & Alexander 2007). However, the beaming modulation by itself might not be enough to identify a binary star, as periodic modulations could be produced by other effects, stellar variability in particular (e.g., Aigrain, Favata & Gilmore 2004).

To overcome this problem, the BEER algorithm (Faigler & Mazeh 2011) searches for stars that show in their light curves a combination of the BEaming effect with two other effects that are produced by a short-period companion — the Ellipsoidal and the Reflection modulations. The ellipsoidal variation (e.g., Morris 1985) is due to the tidal interaction between the two components (see a review by Mazeh (2008)), while the reflection/heating variation (referred to herein as the reflection modulation) is caused by the luminosity of each component that falls on the facing half of its companion (e.g., Wilson 1990; Maxted et al. 2002; Harrison et al. 2003; For et al. 2010; Reed et al. 2010). Detecting the beaming effect together with the ellipsoidal and reflection periodic variations, with the expected relative amplitudes and phases, can indicate the presence of a small non-eclipsing companion. Re-

cently Faigler et al. (2012) reported RV confirmation of seven new non-eclipsing short-period binary systems in the *Kepler* field, with companion minimum masses in the range 0.07–0.4 M_{\odot} , that were discovered by the BEER algorithm.

For brown-dwarfs or planetary companions the beaming effect is even smaller, on the order of 2–50 ppm. Interestingly, several studies were able to detect this minute effect in systems with *transiting brown dwarfs and planets* (Mazeh & Faigler 2010; Shporer et al. 2011; Mazeh et al. 2012; Jackson et al. 2012; Mislis et al. 2012; Barclay et al. 2012), indicating it may be possible to detect such *non-transiting* objects by identifying these effects in their host star light curves.

This paper presents the discovery of Kepler-76b, the first hot Jupiter detected by the BEER algorithm that was subsequently confirmed by TRES and SOPHIE RV spectroscopy. It was identified by the BEER algorithm as a high-priority planetary candidate. Visual inspection of its light curve revealed a V-shaped primary transit and a minute secondary eclipse, combined with beaming, ellipsoidal, and reflection amplitudes, consistent with a massive-planet companion. We noticed later that this star was listed in the *Kepler* eclipsing binary catalog (Prša et al. 2011; Slawson et al. 2011). Based on this information spectroscopic follow-up observations were initiated for this target, which in turn confirmed its planetary nature.

Section 2 presents the BEER search and the initial analysis of the *Kepler* light curve, Section 3 provides the details and results of the spectroscopic observations, Section 4 describes the details and results of the light curve transits and occultations analysis, Section 5 presents the detection of evidence for superrotation in the light curve and Section 6 discusses the implications of, and conclusions from, the findings of this paper.

2. The Photometric BEER search

To identify candidates for low-mass companions we analyzed the *Kepler* raw light curves of the Q2 to Q10 quarters, spanning 831 days. We visually identified 22 time segments that showed instrumental artifacts in the photometry, and ignored data points within those segments, removing a total of 59.9 days of data from the light curves. We also corrected two systematic jumps at *Kepler* times (BJD – 2454833) of 200.32 and 246.19 days. For each light curve, outliers were then removed by 4σ clipping and detrending was performed using a cosine-transform filter, adapted to unevenly spaced data (Mazeh & Faigler 2010; Mazeh et al. 2012), resulting in a cleaned and detrended light curve. We then applied the BEER algorithm to 41,782 stars brighter than 13.7 mag, with *Kepler* Input Catalog

(Brown et al. 2011) radius smaller than $4R_{\odot}$, calculating the Fast Fourier Transform (FFT) based power spectrum of the cleaned and detrended light curve of each star, interpolated over the gaps. Next, in order to avoid spurious peaks at long periods, we divided the full period range of each power spectrum into five sub-ranges: [0.3–1], [1–2], [2–5], [5–10], and [10–20] days, and identified the highest peak within each sub-range. For each of the five peaks we derived the BEER amplitudes and the estimated mass and albedo of the candidate companion (Faigler & Mazeh 2011), assuming the peak corresponds to either the orbital period (beaming and reflection) or half the orbital period (ellipsoidal). The BEER amplitudes were calculated by fitting the data with the modified BEER model suggested by Mazeh et al. (2012), that uses a Lambertian reflection/emission function.

We then selected 26 candidates with the highest signal to noise ratio for the ellipsoidal and beaming amplitudes, and with estimated secondary mass smaller than $60 M_{\text{Jup}}$ and implied albedo smaller than 0.5. One of these candidates was Kepler-76 (*Kepler* Input Catalog number 4570949), for which visual inspection revealed primary and secondary eclipses with depths of about 5×10^{-3} and 1×10^{-4} , respectively. This candidate was also identified as a member of the *Kepler* Eclipsing Binary catalog (Prša et al. 2011). Follow up spectroscopic observations confirmed the companion as a hot Jupiter. In forthcoming papers we will report on our observations of the 26 candidates, additional confirmation of a possible brown dwarf, and the false-positive rate of this sample.

We report here the BEER analysis results for the light curve of Kepler-76 after masking out the transit and occultation data points. We note that in our initial detection the BEER analysis was performed on the unmasked data, but the use a robust-fit function (Holland & Welsch 1977) that identified the transit points as outliers resulted in similar measured BEER amplitudes. Table 1 lists for Kepler-76 the coordinates and stellar properties from the *Kepler* Input Catalog (Brown et al. 2011), revised effective temperature estimate from Pinsonneault et al. (2012), and the results of the BEER analysis. Figure 1 presents a short section of the ‘cleaned’ (Mazeh & Faigler 2010; Faigler & Mazeh 2011) photometric data of the host star, Figure 2 presents the FFT-based power spectrum, and Figure 3 shows the light curve folded with the detected period. It is interesting to notice, by inspecting the cleaned light curves (Figure 1) and the data and residuals r.m.s. (Table 1), that the effects are significantly smaller than the light curve noise, to the point that the detected modulations almost can not be recognized by eye. However, deriving the BEER photometric power spectrum from data with time spans of hundreds of days, produces a prominent detectable peak at the orbital period (Figure 2).

Table 1. Kepler-76: Stellar properties and BEER results

RA	19:36:46.11	Right ascension
DEC	39:37:08.4	Declination
K_p^a [mag]	13.3	<i>Kepler</i> band magnitude
T_{eff}^a [K]	6196	KIC Effective temperature
T_{eff}^b [K]	6409 ± 95	Revised effective temperature
$\log g^a$ [dex]	4.388	Surface gravity
$[m/H]^a$ [dex]	-0.033	Metallicity
R_*^a [R_\odot]	1.12	Primary radius
M_*^c [M_\odot]	1.12	Primary mass
f_3^a	0.056	Average third light fraction
BEER model:		With transit and occultation points masked out
Period [days]	1.5449 ± 0.0007	Orbital period
$T_0 - 2455000^d$ [BJD]	737.49 ± 0.19	Orbital zero phase ephemeris
Ellipsoidal [ppm] ^e	21.5 ± 1.7	Ellipsoidal semi-amplitude
Beaming [ppm] ^e	15.6 ± 2.2	Beaming semi-amplitude
Reflection [ppm] ^e	56.0 ± 2.5	Lambertian reflection/emission semi-amplitude
r.m.s. cleaned data [ppm]	133	Root-mean-square of the cleaned and detrended data
r.m.s. residuals [ppm]	127	Root-mean-square of residuals of data from BEER model

^afrom Kepler Input Catalog

^brevised T_{eff} from Pinsonneault et al. (2012)

^ccalculated from Kepler Input Catalog $\log g$ and R

^d T_0 is the time in which the companion is closest to the observer, assuming a circular orbit

^ecorrected for third light

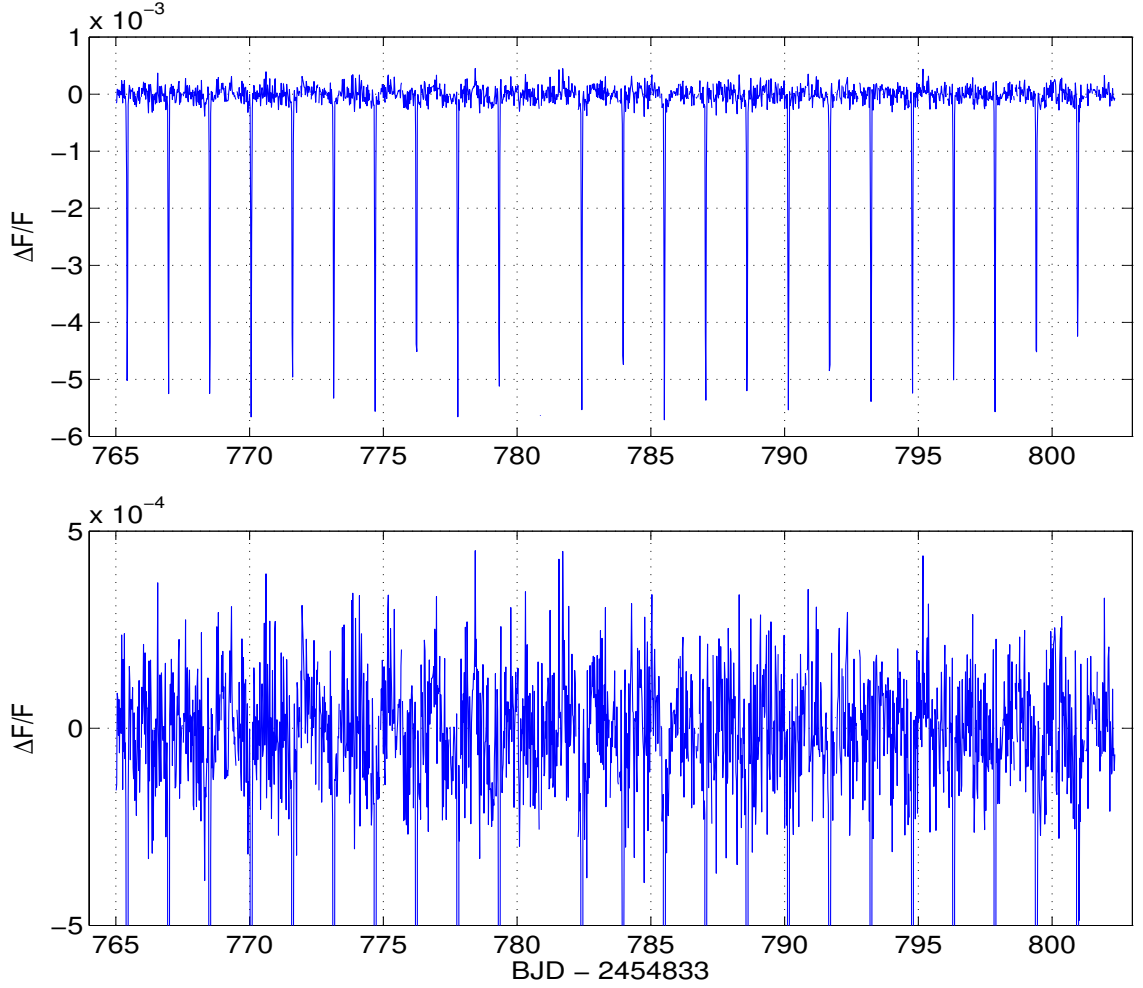


Fig. 1.— The light curve of Kepler-76 for a selected time span of 37 days, after outlier removal and long-term detrending. Top: The untruncated light curve, showing the full depth of the transits. Bottom: The light curve with the core of the transit events truncated. Note the different scales of the two plots. (The transit missing at time 780.9 fell in a short gap in the raw data.)

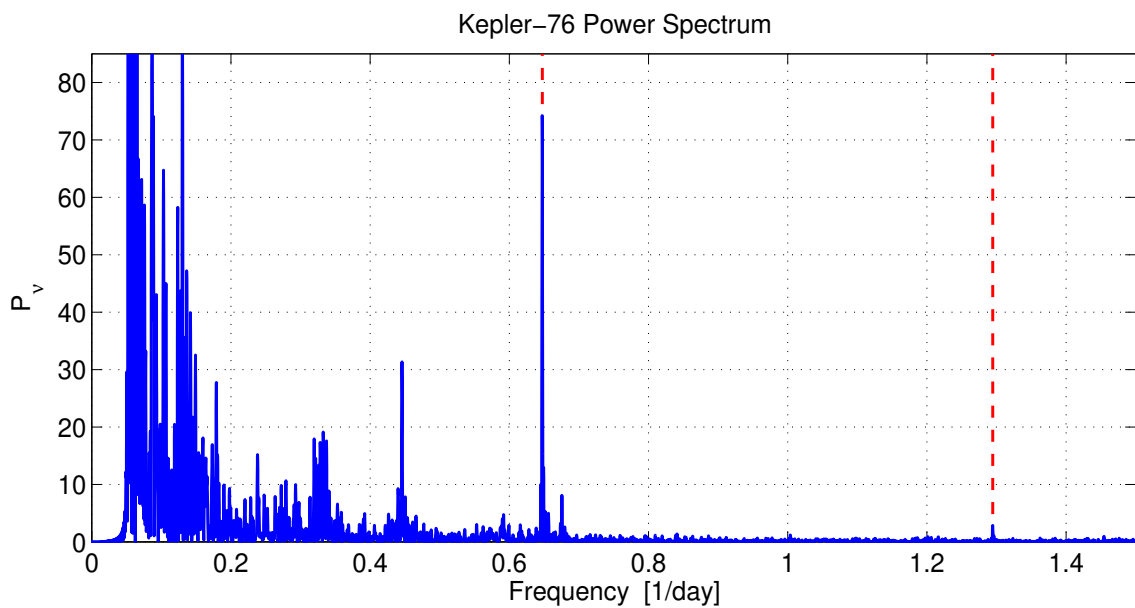


Fig. 2.— The FFT based power spectrum of the detection. The orbital period and half-orbital period peaks are marked by vertical dashed lines. For clarity, only the frequency range of 0–1.5 day^{-1} is plotted, since no significant peak was found for frequencies higher than 1.5 day^{-1} .

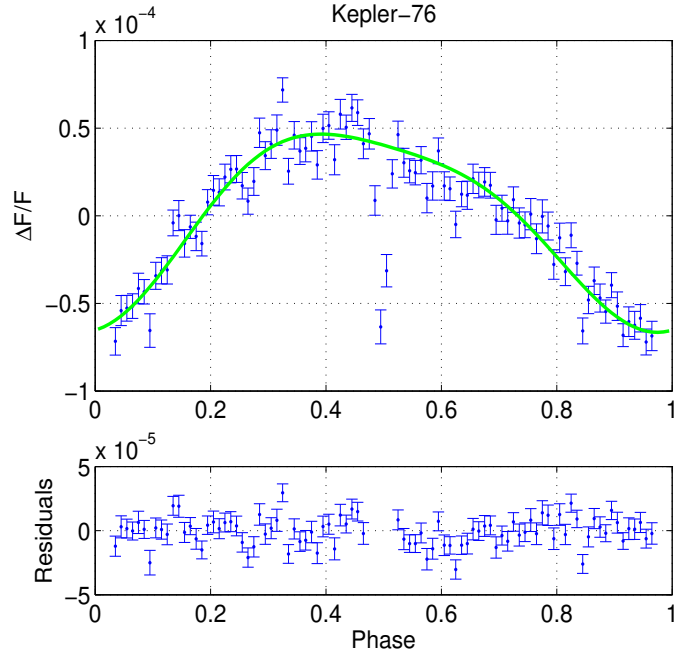


Fig. 3.— The folded cleaned light curve binned into 100 bins. Phase zero is when the companion is closest to the observer, while phase 0.5 is when the primary is closest to the observer, assuming a circular orbit. The error bars represent 1σ uncertainties of the median value of each bin, based on the scatter of data points within that bin. The line presents the BEER model. The residuals of the data from the model are plotted in the bottom panel. For clarity, the primary eclipse was removed. The secondary eclipse is clearly visible at phase 0.5 of the plot.

3. Spectroscopic observations

Spectroscopic observations of the candidate were obtained between 29 May and 6 October 2012 with the Tillinghast Reflector Echelle Spectrograph (TRES; Fűrész 2008) mounted on the 1.5-m Tillinghast Reflector at the Fred Lawrence Whipple Observatory operated by the Smithsonian Astrophysical Observatory (SAO) on Mount Hopkins in Southern Arizona, using the medium resolution fiber at a spectral resolution of 44,000, covering a spectral range from 385 to 910 nm. Exposures of a Thorium-Argon hollow-cathode lamp immediately before and after each exposure were used for wavelength calibration. The spectra were extracted and rectified to intensity vs. wavelength using standard procedures developed by Lars Buchhave (Buchhave et al. 2010).

Additional spectroscopic observations were obtained between 17 July and 1 August 2012 with the SOPHIE spectrograph (Perruchot et al. 2008; Bouchy et al. 2009, 2013) mounted on the 1.93-m telescope at Observatoire de Haute-Provence, France, using the High Efficiency mode ($R \sim 39,000$ at 550 nm) of the instrument. Spectra were extracted with the online standard pipeline.

Following a method similar to the Stellar Parameter Classification method (SPC, Buchhave et al. 2012), the atmospheric parameters of Kepler-76 were determined from the SOPHIE spectra by cross-correlating the observed spectral regions not affected by telluric lines against a library of synthetic spectra (Hauschildt et al. 1999), with varying values of effective temperature T_{eff} , surface gravity $\log g$, metallicity $[m/H]$ and rotational velocity $v \sin i$. For each of the observed spectra we derived the best set of parameters that yielded the highest correlation. This was done by fitting a second degree polynomial to the maximum correlation as function of each parameter around the synthetic spectrum that yielded the best correlation. The final parameter values for a star were taken as the mean of the parameter values derived for each observed spectrum of that star, weighted proportionally to the inverse of the scatter of the maximum around the fitted polynomial.

The Phoenix library of synthetic spectra we used spans the following intervals in atmospheric parameters: $3000\text{K} < T_{\text{eff}} < 10000\text{K}$, $-0.5 < \log g < 5.5$ (cgs), and $-1.5 < [m/H] < +0.5$. The spacing in T_{eff} is 100K for $T_{\text{eff}} < 7000\text{K}$, and 200K elsewhere. The spacing in $\log g$ and $[m/H]$ is 0.5 dex. The interval and spacing of $v \sin i$ values in our algorithm are free parameters set by the user, since each synthetic spectrum chosen from the library is convolved with a rotational profile $G(v)$ (e.g., Gray (2005), p. 465; Santerne et al. (2012)) and a Gaussian representing the instrumental broadening of the lines, just before calculating cross-correlation function.

The cross-correlation was performed using TODMOR (Zucker & Mazeh 1994; Zucker et al.

2003, 2004) — a two-dimensional correlation algorithm, assuming the light contribution of the secondary is negligible. In TODMOR, the cross-correlation functions are calculated separately for each echelle order, and then combined to a single cross-correlation function according the scheme proposed by Zucker et al. (2003). The atmospheric parameters found this way are listed in Table 2. The relatively large uncertainties result mainly from the addition of possible systematic errors (see e.g., Bruntt et al. 2010, 2012; Torres et al. 2012).

The primary mass was estimated using the atmospheric parameters derived from the spectra and a grid of Y^2 stellar isochrones (Yi et al. 2001; Demarque et al. 2004). This was done by taking into account all age and mass values that fall into the ellipsoid in the $(T_{\text{eff}}, \log g, [Fe/H])$ space defined by the atmospheric parameters and their errors. To illustrate the process Figure 4 shows two sets of Y^2 stellar isochrones of 0.2, 0.4, 1, 2, 4, 8, and 10 Gyr — one for $[Fe/H] = 0.05$ (solid lines) and one for $[Fe/H] = -0.27$ (dashed lines). The ellipse defined by the estimated T_{eff} and $\log g$ and their uncertainties is also shown. A lower limit of 0.2 Gyr on the stellar age was set to ignore possible pre-main sequence solutions. This procedure yielded a mass estimate of $1.20 \pm 0.09 M_{\odot}$. Following Basu et al. (2012) we have conservatively doubled the mass errors to take into account possible uncertainties in stellar model parameters.

Radial velocities were derived for the TRES observations in two different ways, as described in detail by Faigler et al. (2012). First, we derived absolute velocities using cross-correlations of the observed spectra against the template from our library of synthetic spectra that yielded the best match (with $T_{\text{eff}} = 6000\text{K}$, $\log g = 4.0$ cgs, $v \sin i = 12 \text{ km s}^{-1}$ and solar metallicity). The absolute velocity analysis used just the spectral order containing the MgIb triplet and was calibrated using IAU RV standard stars. With the goal of achieving better precision we also derived velocities using about two dozen spectral orders, correlating the individual observations against a template based on the strongest exposure. Thus the multi-order velocities are relative to the observation chosen as the template. They are reported in Table 3.

For the SOPHIE observations, radial velocities were derived by computing the weighted cross-correlation function (CCF) of the spectra with a numerical spectral mask of a G2V star (Baranne et al. 1996; Pepe et al. 2002). For the last five exposures, which were contaminated by scattered moon light, we subtracted the sky using the fiber B spectrum (Santerne et al. 2009), before deriving the radial velocities. Table 3 lists the radial-velocity measurements and their uncertainties.

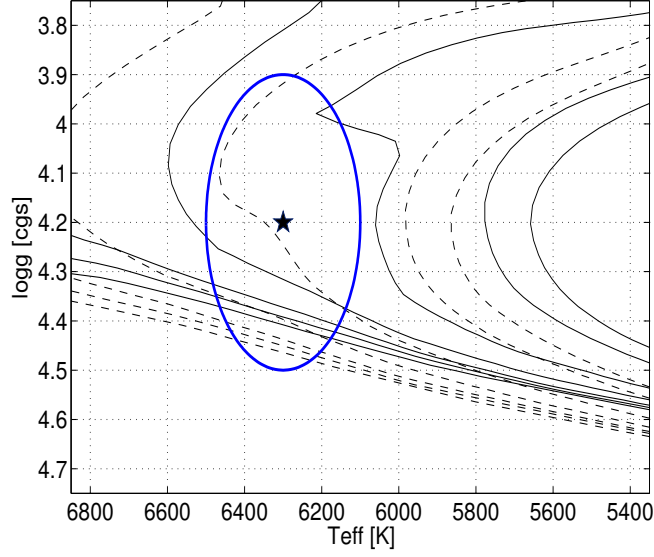


Fig. 4.— Y^2 stellar isochrones, from Demarque et al. (2004), of 0.2–10 Gyr for metallicities $[Fe/H] = 0.05$ (solid lines) and $[Fe/H] = -0.27$ (dashed lines). The estimated T_{eff} and $\log g$ of Kepler-76 with their uncertainties are marked by a star and an ellipse.

Table 2: Atmospheric parameters of Kepler-76

T_{eff} [K]	6300 ± 200
$\log g$ [dex]	4.2 ± 0.3
$[m/H]$ [dex]	-0.1 ± 0.2
$v \sin i$ [km s $^{-1}$]	6.5 ± 2
M_* [M_{\odot}]	1.2 ± 0.2

Table 3: Radial-velocity measurements

Time [BJD–2456000]	RV [km s $^{-1}$]	σ [km s $^{-1}$]	Instrument
76.930366	0.581	0.069	TRES
83.895818	0.161	0.110	TRES
84.868623	0.546	0.072	TRES
87.836880	0.607	0.103	TRES
107.916759	0.586	0.098	TRES
115.796005	0.727	0.114	TRES
117.775394	0.100	0.082	TRES
207.682884	0	0.069	TRES
126.378842	-4.999	0.036	SOPHIE
128.575439	-5.597	0.036	SOPHIE
129.562543	-5.081	0.056	SOPHIE
130.416149	-5.560	0.091	SOPHIE
131.389038	-5.341	0.061	SOPHIE
137.536798	-5.196	0.132	SOPHIE
138.488304	-5.194	0.057	SOPHIE
139.470933	-5.615	0.080	SOPHIE
140.470516	-4.992	0.114	SOPHIE
141.450747	-5.171	0.082	SOPHIE

The first RV measurements of Kepler-76 showed variability consistent with the photometric orbital phase, so we continued observations in order to allow an orbital solution independent of the BEER analysis. The derived eccentricity of the solution was statistically indistinguishable from zero, so we reran the solution with eccentricity fixed to zero. Figure 5 shows the follow-up RV measurements and the velocity curve for the orbital solution, folded with the period found, and the top section of Table 4 lists the derived orbital elements for the independent RV solution. The center-of-mass velocities γ_T and γ_S for the independent RV sets from TRES and SOPHIE differ by 5.68 km s^{-1} . This is because the TRES velocities are relative to the strongest observation, while the SOPHIE velocities are meant to be on an absolute scale. If the absolute TRES velocities derived using the Mg b order are used instead of the relative velocities, $\gamma_T = -5.18 \text{ km s}^{-1}$, quite close to the SOPHIE value of $\gamma_S = -5.31 \text{ km s}^{-1}$. For the joint analysis reported below, the two independent velocity sets were shifted to a common zeropoint using the γ velocities reported in Table 4.

Next, in order to obtain a combined solution from photometry and RV measurements, we reran the RV model using the photometric period and ephemeris, with their uncertainties, as priors. The bottom section of Table 4 lists the orbital elements derived from this photometry-constrained RV solution, and the estimated minimum secondary mass, $M_p \sin i$.

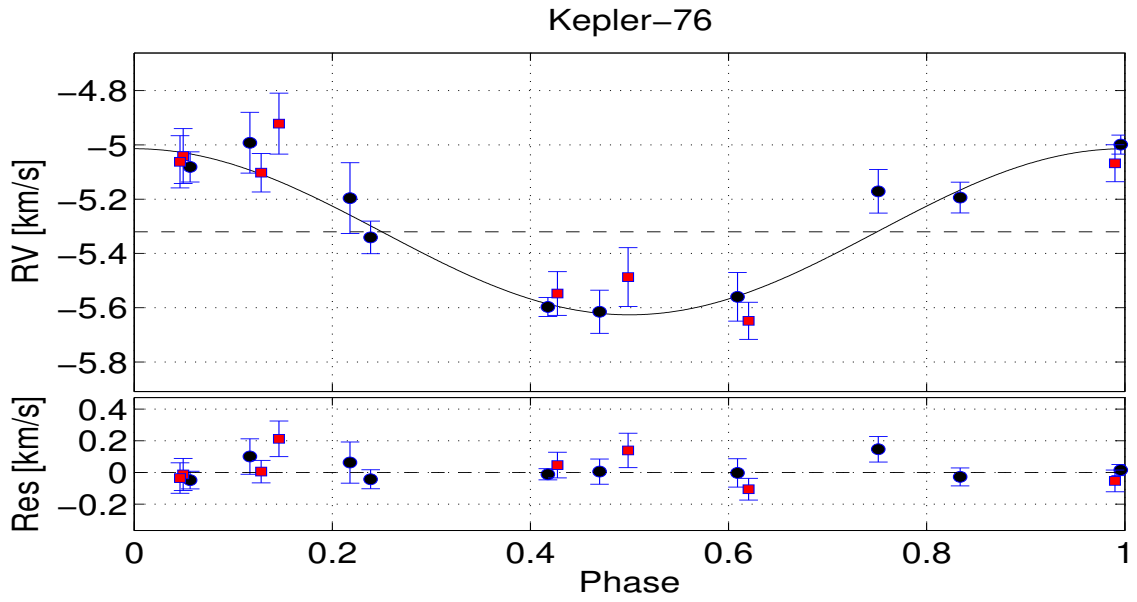


Fig. 5.— The RV measurements folded at the derived orbital period. In the top panel, the solid line presents the photometry-constrained orbital RV model and the horizontal-dashed line indicates the center-of-mass velocity. Circles denote SOPHIE RV points and squares denote TRES RV points. The residuals are plotted at the bottom panel. Note the different scales of the upper and lower panels.

Table 4. Orbital elements based on RV measurements

N	18	Number of RV measurements
span [days]	130.8	Time span of measurements
Independent RV solution:		
$T_0 - 2456000$ ^a [BJD]	126.76 ± 0.03	Orbital ephemeris
P [days]	1.5474 ± 0.0021	Orbital period
γ_T [km s ⁻¹]	0.365 ± 0.042	Zero point velocity of TRES
γ_S [km s ⁻¹]	-5.315 ± 0.019	Zero point velocity of SOPHIE
K_{RV} [km s ⁻¹]	0.308 ± 0.020	Radial velocity semi-amplitude
RV solution constrained by the photometric period and ephemeris:		
$T_0 - 2456000$ ^a [BJD]	126.77 ± 0.023	Orbital ephemeris
P [days]	1.5450 ± 0.0005	Orbital period
γ_T [km s ⁻¹]	0.328 ± 0.032	Zero point velocity of TRES
γ_S [km s ⁻¹]	-5.320 ± 0.020	Zero point velocity of SOPHIE
K_{RV} [km s ⁻¹]	0.306 ± 0.020	Radial velocity semi-amplitude
$M_p \sin i$ [M_{Jup}]	1.96 ± 0.25	Minimum companion mass

^a T_0 is the time in which the companion is closest to the observer

4. Photometric modeling of the light curve

For a more complete photometric analysis of this transiting hot Jupiter we used the *Kepler* light curves of the Q2 to Q13 quarters, spanning 1104 days. First we fitted the cleaned and detrended data with the BEER model while masking out data points in or around the transits and occultations. The fitted amplitudes, after correction for a third light using the KIC estimate, are listed in Table 6. We then subtracted the BEER model from the data and analyzed the data points in and around the transits and occultations. For that we ran a Markov chain Monte Carlo (MCMC) analysis, while fitting the transit data points using a long-cadence integrated Mandel & Agol (2002) model with quadratic limb darkening, assuming a circular orbit. The model limb darkening coefficients could not be constrained, so we kept them fixed at values interpolated from Claret & Bloemen (2011) using the stellar parameters derived from spectroscopy. We then fitted the occultation data keeping the geometric parameters derived from the transit fixed, and assuming a linear limb darkening coefficient of 0.5 for the planet, while looking for the occultation depth that best fits the data.

Figure 6 presents the cleaned and detrended data points and the best-fit Mandel & Agol (2002) model combined with the BEER model, both folded at the orbital period. Table 5 lists the priors and the MCMC medians and 1σ uncertainties of the posterior parameters. We note here that the orbital period P and time of primary transit T_0 listed in Table 5 were derived from the transit data points, thus yielding high-accuracy estimates. The same parameters, listed in Table 1, were derived from the out-of-transit data, thus yielded much lower-accuracy estimates. The T_0 values listed in both tables were not corrected for the *Kepler* timing error (http://archive.stsci.edu/kepler/timing_error.html), which should be taken in account when comparing them to non-*Kepler* observations.

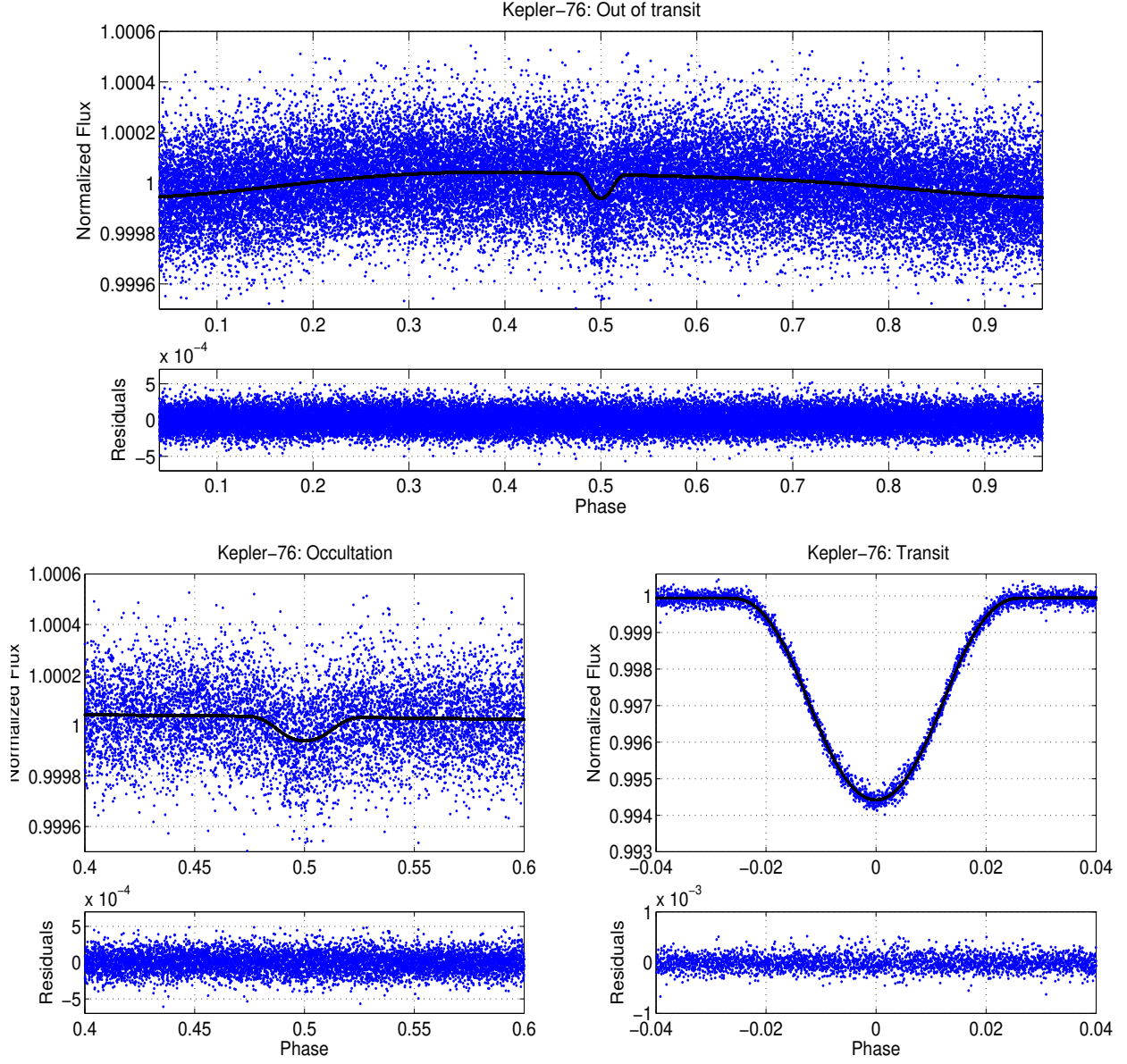


Fig. 6.— Kepler-76 cleaned and detrended data points and best-fit model, both folded at the orbital period. In the top panel of each plot, the solid line presents the best-fit model, and the dots present the data points. The residuals are plotted in the bottom panel. Note the different scales of the upper and lower panel of each plot.

Table 5. Photometric light curve transit and occultation model

Parameter	Median and 1σ uncertainty	
Priors:		
M_* [M_\odot]	1.2 ± 0.2	Primary mass
a_*	0.313	Star linear limb darkening coefficient
b_*	0.304	Star quadratic limb darkening coefficient
a_p	0.5	Planet linear limb darkening coefficient
b_p	0	Planet quadratic limb darkening coefficient
f_3	0.056	Average third light fraction (From KIC)
Posteriors:		
T_0 [BJD]	$2454966.54811 \pm 0.00007$	Time of primary transit
Period [days]	$1.54492875 \pm 0.00000027$	Orbital period
i [deg]	78.0 ± 0.2	Orbital inclination
R_*/a	0.221 ± 0.003	Fractional primary radius
R_p/a	0.0214 ± 0.0008	Fractional planet radius
d_2 [ppm]	98.9 ± 7.1	Occultation depth
Derived Parameters:		
ρ_*/ρ_\odot	0.522 ± 0.019	Primary density relative to the Sun density
R_* [R_\odot]	1.32 ± 0.08	Primary radius
R_p [R_{Jup}]	1.25 ± 0.08	Planet radius
b	0.944 ± 0.011	Impact parameter

5. Inflated beaming amplitude and planet equatorial super-rotating jet

The spectroscopic RV observations and the light curve transit and occultation analysis yielded independent orbital solutions with ephemeris and period nicely consistent with the BEER ephemeris and period. To compare the measured RV amplitude with the beaming-based predicted RV amplitude, one needs to evaluate the α_{beam} factor, which corrects for the Doppler shift of the stellar spectrum relative to the observed band of the telescope (Rybicki & Lightman 1979; Faigler & Mazeh 2011).

To estimate the α_{beam} value, we used spectra from the library of Castelli & Kurucz (2004) models close to the estimated temperature, metallicity and gravity of the primary star, numerically shifting them relative to the *Kepler* response function, while taking into account the photon counting nature of *Kepler* (Loeb & Gaudi 2003; Bloemen et al. 2011; Faigler et al. 2012). For clarity we note that by definition $\alpha_{\text{beam}} = \frac{3-\alpha}{4} = \frac{\langle B \rangle}{4}$, where α is the power-law index used by Loeb & Gaudi (2003) and $\langle B \rangle$ is the photon weighted bandpass-integrated beaming factor used by Bloemen et al. (2011). The result of this calculation gave $\alpha_{\text{beam}} = 0.92 \pm 0.04$, resulting in an RV semi-amplitude of $K_{\text{beam}} = 1.11 \pm 0.17 \text{ km s}^{-1}$. The RV semi-amplitude predicted from the beaming effect was 3.5 times larger than the measured amplitude, with a difference significance of about 4.5σ between the two.

A possible explanation for this inflated photometric beaming amplitude might be a phase shift of the reflection signal, due to the superrotation phenomenon, which involves eastward advection of gas by an equatorial super-rotating jet within the atmosphere of a co-rotating companion. Showman & Guillot (2002) predicted through a 3D atmospheric circulation model that tidally-locked, short period planets develop a fast eastward, or *superrotating*, jet stream that extends from the equator to latitudes of typically $20^\circ - 60^\circ$. They showed that in some cases (depending on the imposed stellar heating and other factors) this jet causes an eastward displacement of the hottest regions by $10^\circ - 60^\circ$ longitude from the substellar point, resulting in a phase shift of the thermal emission phase curve of the planet. This prediction was confirmed by Knutson et al. (2007, 2009) through *Spitzer* infrared observations of HD 189733, which indicated a phase shift of $16^\circ \pm 6^\circ$ in the $8 \mu\text{m}$ band and $20^\circ - 30^\circ$ in the $24 \mu\text{m}$ band.

In general, what we call a reflection modulation is actually the light scattered off the planet in combination with radiation absorbed and later thermally re-emitted at different wavelengths. The two processes are controlled by the Bond albedo, $0 < A_B < 1$, and the day–night heat redistribution efficiency, $0 < \epsilon < 1$, which can be constrained only if observations of the phase modulation or the secondary eclipse are available in different wavelengths (Cowan & Agol 2011). This makes it impossible to distinguish between reflected and re-radiated photons from the single band *Kepler* light curve we have in hand. Cowan & Agol

(2011) discuss HAT-P-7 as an example, and show that its *Kepler* light curve can be explained as mostly reflected light at one limit, to mostly thermal emission at the other limit, with an entire range of models between them being consistent with the light curve. This is important for the current discussion, as we expect superrotation to shift only the thermal re-emission, while leaving the scattered light component unshifted.

To estimate the maximum fraction of the reflection amplitude originating from thermal re-emission in our case, we follow Cowan & Agol (2011) and estimate the no albedo, no redistribution, effective day side temperature $T_{\epsilon=0} \approx 2670K$, which translates in the *Kepler* band to a maximum reflection amplitude $A_{\text{ref}} \approx 37$ ppm. This means that the measured amplitude of ≈ 50 ppm can be explained mostly by thermal re-emission. The actual fraction of thermal emission in this case is probably smaller, but this calculation illustrates that the fraction of thermal emission in the visual *Kepler* light curve phase modulation may be significant, making it a worthy effort to look for a superrotation phase shift in the light curve.

We suggest here, that if such a phase shift is present in the *Kepler* light curve, it will show up in our phase curve model mainly as an inflated beaming amplitude. To illustrate that we consider a simple superrotation model consisting of a phase-shifted geometric reflection/emission combined with a beaming modulation,

$$\mathcal{M}_{SR} = -A_{\text{ref}} \cos(\phi + \delta_{SR}) + A_{\text{beam}} \sin \phi = -A_{\text{ref}} \cos \delta_{SR} \cos \phi + (A_{\text{beam}} + \underline{A_{\text{ref}} \sin \delta_{SR}}) \sin \phi, \quad (1)$$

where A_{ref} is the reflection/emission semi-amplitude, A_{beam} is the beaming semi-amplitude, ϕ is the orbital phase relative to mid-transit, and δ_{SR} is the superrotation phase shift angle. This model suggests that if a phase shift is present *and* the reflection amplitude is larger than, or of the order of, the beaming amplitude, the underlined term in Eq. 1 may add substantially to the amplitude of the $\sin \phi$ modulation, mimicking an inflated beaming effect.

To test our conjecture that the beaming/ellipsoidal inconsistency is a result of a superrotation phase shift of the reflection/emission phase modulation, we fitted the data using the derived system parameters (Tables 5 and 2) and the BEER effects equations (Faigler & Mazeh 2011), while looking for the planetary mass, geometric albedo, and phase shift of the Lambertian phase function that minimized the χ^2 of the fit. Adding the phase shift parameter to the model resulted in a decrease of the χ^2 value by 90, relative to the no-phase-shift model, indicating a substantially better agreement of the data with a model that combines beaming, ellipsoidal and a phase shifted Lambertian reflection. An F-test shows that fitting the data while allowing for a phase shift, as opposed to the no-phase-shift null model, yields a better fit with a confidence level better than 9σ . Table 6 lists the amplitudes derived by the BEER analysis, the planetary mass derived directly from the beaming versus the ellipsoidal amplitudes, and the spectroscopic RV derived planetary mass. The table then

lists the planetary mass, phase-shift angle and geometric albedo resulting from the superrotation model. The superrotation phase shift estimate is small and well within the theoretical limit of 60° predicted by Showman & Guillot (2002). In addition, the derived planetary mass estimate is well within the 1σ range of the RV measured planetary mass, indicating that assuming superrotation resolves the inconsistency and provides a good estimate for the planetary mass, derived *solely* from the *Kepler* photometry, given a good stellar model.

Table 6. BEER amplitudes, planetary mass, and superrotation phase shift angle

BEER model:		
Ellipsoidal [ppm] ^a	21.1 ± 1.7	Ellipsoidal semi-amplitude
Beaming [ppm] ^a	13.5 ± 2.0	Beaming semi-amplitude
Reflection [ppm] ^a	50.4 ± 2.0	Reflection semi-amplitude
a_{2s} [ppm] ^a	-2.7 ± 1.0	$\sin 2\phi$ coefficient
<hr/>		
$M_{p,beam}$ [M_{Jup}]	7.2 ± 1.4	Planetary mass derived from beaming
$M_{p,ellip}$ [M_{Jup}]	2.1 ± 0.4	Planetary mass derived from ellipsoidal
$M_{p,RV}$ [M_{Jup}]	2.00 ± 0.26	Planetary mass measured by spectroscopic RV
<hr/>		
Superrotation phase-shift model solution:		
$M_{p,SR}$ [M_{Jup}]	2.1 ± 0.4	Planetary mass
δ_{SR} [deg]	10.3 ± 2.0	Superrotation phase shift angle
A_g	0.23 ± 0.02	Geometric albedo
N	31468	Number of data points
χ^2	31465	χ^2 of a model allowing for a phase shift
χ^2_{null}	31555	χ^2 of a zero phase shift model (null model)

^acorrected for third light

6. Discussion

This paper presents a new hot-Jupiter companion, Kepler-76b, initially identified by the BEER algorithm, and later confirmed by spectroscopic observations. The BEER detection was based on the photometrically measured amplitudes of the BEaming, Ellipsoidal and Reflection effects, that were consistent with a planetary companion. This is just the third confirmed planet in the *Kepler* field, after HAT-P-7b (Welsh et al. 2010) and TrES-2b (Barclay et al. 2012), that its host light curve exhibits the three phase curve effects, and is the faintest of the three stars. It is also one of a few confirmed grazing exoplanets, showing a V-shaped transit and a partial occultation.

We have identified an inconsistency between the beaming amplitude and the spectroscopically measured radial velocity. Similar inconsistencies between the planetary mass derived from the beaming amplitudes and the mass derived from the ellipsoidal amplitude were noticed previously by several authors for KOI-13 (Mazeh et al. 2012; Shporer et al. 2011) and TrES-2 (Barclay et al. 2012). We suggest here that these inconsistencies can be explained by a phase shift of the planetary thermal modulation due to the equatorial superrotation phenomena predicted by Showman & Guillot (2002) and later observed by Knutson et al. (2007, 2009) in the infrared for HD 189733. In such cases we should be able to measure the superrotation phase-shift angle from the visual band *Kepler* light curve of the system. As we do not expect scattered light to exhibit such a phase shift, visual band detection of the superrotation phase shift may yield a constraint on the ratio of scattered light to thermally re-emitted light from the planet.

Finally, we wish to briefly comment on the sensitivity of the BEER algorithm. The detection presented here exhibits the lowest-mass companion identified so far by the algorithm, indicating its possible current detection limit. As we require that a BEER candidate must show statistically significant beaming *and* ellipsoidal effects to be considered valid, we choose here the minimum of the semi-amplitudes of the two effects as the BEER detectability parameter of a planet. To estimate our ability to detect more planets and brown dwarfs, Figure 7 presents the calculated value of this parameter, using the Faigler & Mazeh (2011) equations, for known exoplanets of mass higher than $0.5M_{\text{Jup}}$ and period shorter than 30 days, as of January 2013 (<http://exoplanet.eu/>), together with the measured value for Kepler-76b. The figure shows that there are six transiting and one RV detected planets with calculated amplitudes higher than that of Kepler-76b, suggesting that these systems could have been detected by the BEER algorithm, if their stellar and instrumental noise were similar to that of Kepler-76. It is also apparent that further enhancement of the algorithm sensitivity could significantly increase the number of potentially detectable planets. Given the fact that BEER can detect similar *non-transiting* objects, we expect to find more objects

once we improve our detection threshold.

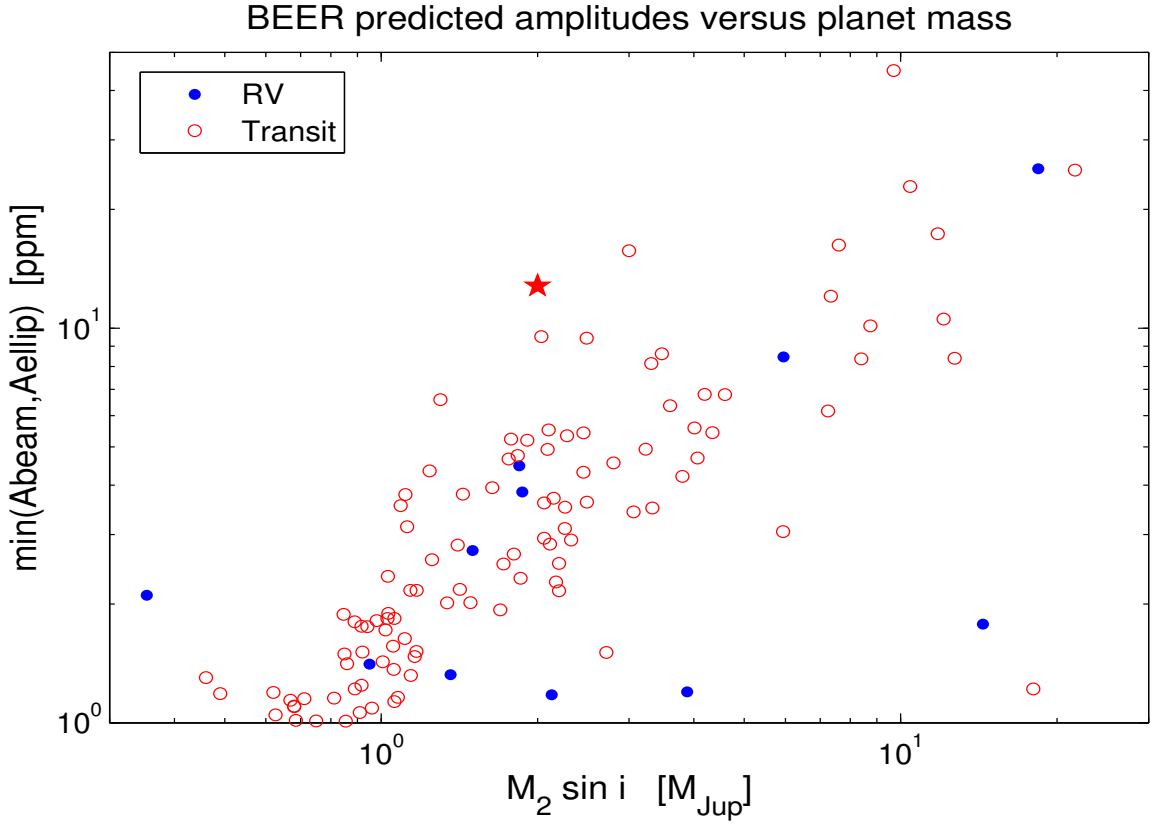


Fig. 7.— The minimum of the predicted beaming and ellipsoidal semi-amplitudes, as a function of the secondary mass, for known exoplanets of mass higher than $0.5M_{\text{Jup}}$ and period shorter than 30 days. Blue dots mark exoplanets detected by RV, red circles mark exoplanets detected by transit, and the red star marks the measured amplitude of Kepler-76b.

We are indebted to Shay Zucker for numerous helpful discussions, and to Ignasi Ribas for discussing the thermal phase shift. We thank the referee Steven Bloemen for his valuable remarks and suggestions, and especially for his comment about the α_{beam} calculation. The research leading to these results has received funding from the European Research Council under the EU’s Seventh Framework Programme (FP7/(2007-2013)/ ERC Grant Agreement No. 291352). This research was supported by the ISRAEL SCIENCE FOUNDATION (grant No. 1423/11). We feel deeply indebted to the team of the Kepler mission, that enabled us to search and analyze their unprecedentedly accurate photometric data. All the photometric data presented in this paper were obtained from the Multimission Archive at the Space Telescope Science Institute (MAST). STScI is operated by the Association of Universities for Research in Astronomy, Inc., under NASA contract NAS5-26555. Support for MAST for non-HST data is provided by the NASA Office of Space Science via grant NNX09AF08G and by other grants and contracts. We thank the Kepler mission for partial support of the spectroscopic observations under NASA Cooperative Agreement NNX11AB99A with the Smithsonian Astrophysical Observatory, DWL PI. We are indebted to Andrew H. Szentgyorgyi, who led the TRES project, and to Gabor Fűrész for his many contributions to the success of the instrument. We thank Robert P. Stefanik, Perry Berlind, Gilbert A. Esquerdo, and Michael L. Calkins for obtaining the TRES observations, and Allyson Bieryla and Jessica Mink for help with the data analysis. This paper is based in part on observations made at Observatoire de Haute Provence (CNRS), France. We are grateful to the OHP director and team for the allocation of the SOPHIE observing time. We are also thankful for the help of the night assistants, that enabled us to obtain the spectra presented here. OHP observations were supported by the OPTICON network. OPTICON has received research funding from the European Community’s Seventh Framework Programme.

Facilities: FLWO:1.5m(TRES) , OHP:1.93m(SOPHIE)

REFERENCES

- Aigrain, S., Favata, F., & Gilmore, G. 2004, A&A, 414, 1139
- Auvergne, M., et al. 2009, A&A, 506, 411
- Baranne, A., Queloz, D., Mayor, M., et al. 1996, A&AS, 119, 373
- Barclay, T., Huber, D., Rowe, J. F., et al. 2012, ApJ, 761, 53
- Basu, S., Verner, G. A., Chaplin, W. J., & Elsworth, Y. 2012, ApJ, 746, 76
- Bloemen, S., et al. 2011, MNRAS, 410, 1787

- Bloemen, S., Marsh, T. R., Degroote, P., et al. 2012, MNRAS, 422, 2600
- Bouchy, F., Hébrard, G., Udry, S., et al. 2009, A&A, 505, 853
- Bouchy, F., Díaz, R. F., Hébrard, G., et al. 2013, A&A, 549, A49
- Breton, R. P., Rappaport, S. A., van Kerkwijk, M. H., & Carter, J. A. 2012, ApJ, 748, 115
- Brown, T. M., Latham, D. W., Everett, M. E., & Esquerdo, G. A. 2011, arXiv:1102.0342
- Bruntt, H., Bedding, T. R., Quirion, P.-O., et al. 2010, MNRAS, 405, 1907
- Bruntt, H., Basu, S., Smalley, B., et al. 2012, MNRAS, 423, 122
- Buchhave, L. A., et al. 2010, ApJ, 720, 1118
- Buchhave, L. A., Latham, D. W., Johansen, A., et al. 2012, Nature, 486, 375
- Carter, J. A., Rappaport, S., & Fabrycky, D. 2011, ApJ, 728, 139
- Castelli, F., & Kurucz, R. L. 2004, arXiv:astro-ph/0405087
- Claret, A., & Bloemen, S. 2011, A&A, 529, A75
- Cowan, N. B., & Agol, E. 2011, ApJ, 729, 54
- Demarque, P., Woo, J.-H., Kim, Y.-C., & Yi, S. K. 2004, ApJS, 155, 667
- Faigler, S., & Mazeh, T. 2011, MNRAS, 1106
- Faigler, S., Mazeh, T., Quinn, S. N., Latham, D. W., & Tal-Or, L. 2012, ApJ, 746, 185
- For, B.-Q., et al. 2010, ApJ, 708, 253
- Fűrész, G., Ph.D. thesis, University of Szeged, Hungary
- Gray, D. F. 2005, "The Observations and Analysis of Stellar Photospheres, 3rd Edition, by D. F. Gray. ISBN 0521851866. Cambridge, UK: Cambridge University Press, 2005."
- Harrison, T. E., Howell, S. B., Huber, M. E., Osborne, H. L., Holtzman, J. A., Cash, J. L., & Gelino, D. M. 2003, AJ, 125, 2609
- Hauschildt, P. H., Allard, F., & Baron, E. 1999, ApJ, 512, 377
- Holland, P. W., & Welsch R. E. 1977, Communications in Statistics: Theory and Methods, A6, 813

- Jackson, B. K., Lewis, N. K., Barnes, J. W., et al. 2012, *ApJ*, 751, 112
- Kipping, D. M., & Spiegel, D. S. 2011, arXiv:1108.2297
- Knutson, H. A., Charbonneau, D., Allen, L. E., et al. 2007, *Nature*, 447, 183
- Knutson, H. A., Charbonneau, D., Cowan, N. B., et al. 2009, *ApJ*, 690, 822
- Koch, D. G., et al. 2010, *ApJ*, 713, L79
- Loeb, A., & Gaudi, B. S. 2003, *ApJ*, 588, L117
- Mandel, K., & Agol, E. 2002, *ApJ*, 580, L171
- Maxted, P. F. L., Marsh, T. R., Heber, U., Morales-Rueda, L., North, R. C., & Lawson, W. A. 2002, *MNRAS*, 333, 231
- Mazeh, T. 2008, *EAS Publications Series*, 29, 1
- Mazeh, T., & Faigler, S. 2010, *A&A*, 521, L59
- Mazeh, T., Nachmani, G., Sokol, G., Faigler, S., & Zucker, S. 2012, *A&A*, 541, A56
- Mislis, D., Heller, R., Schmitt, J. H. M. M., & Hodgkin, S. 2012, *A&A*, 538, A4
- Morris, S. L. 1985, *ApJ*, 295, 143
- Pepe, F., Mayor, M., Galland, F., et al. 2002, *A&A*, 388, 632
- Perruchot, S., Kohler, D., Bouchy, F., et al. 2008, *Proc. SPIE*, 7014,
- Pinsonneault, M. H., An, D., Molenda-Żakowicz, J., et al. 2012, *ApJS*, 199, 30
- Prša, A., et al. 2011, *AJ*, 141, 83
- Reed, M. D., et al. 2010, *Ap&SS*, 329, 83
- Rowe, J., Borucki, W. J., Howell, S. B., et al. 2011, *Bulletin of the American Astronomical Society*, 43, #103.04
- Rybicki, G. B., & Lightman, A. P. 1979, *Radiative Processes in Astrophysics* (New York: Wiley)
- Santerne, A., Moutou, C., Bouchy, F., Hébrard, G., & Deleuil, M. 2009, *SF2A-2009: Proceedings of the Annual meeting of the French Society of Astronomy and Astrophysics*, 21

- Santerne, A., Moutou, C., Barros, S. C. C., et al. 2012, *A&A*, 544, L12
- Showman, A. P., & Guillot, T. 2002, *A&A*, 385, 166
- Shporer, A., Jenkins, J. M., Rowe, J. F., et al. 2011, *AJ*, 142, 195
- Slawson, R. W., Prša, A., Welsh, W. F., et al. 2011, *AJ*, 142, 160
- Torres, G., Fischer, D. A., Sozzetti, A., et al. 2012, *ApJ*, 757, 161
- Weiss, L. M., Marcy, G., Orosz, J., et al. 2012, American Astronomical Society Meeting Abstracts #220, 220, #523.19
- Welsh, W. F., Orosz, J. A., Seager, S., et al. 2010, *ApJ*, 713, L145
- Wilson, R. E. 1990, *ApJ*, 356, 613
- van Kerkwijk, M. H., Rappaport, S. A., Breton, R. P., Justham, S., Podsiadlowski, P., & Han, Z. 2010, *ApJ*, 715, 51
- Yi, S., Demarque, P., Kim, Y.-C., et al. 2001, *ApJS*, 136, 417
- Zucker, S., & Mazeh, T. 1994, *ApJ*, 420, 806
- Zucker, S., Mazeh, T., Santos, N. C., Udry, S., & Mayor, M. 2003, *A&A*, 404, 775
- Zucker, S., Mazeh, T., Santos, N. C., Udry, S., & Mayor, M. 2004, *A&A*, 426, 695
- Zucker, S., Mazeh, T., & Alexander, T. 2007, *ApJ*, 670, 1326